Solar RRL

WILEY VCH

Solar RRL

RESEARCH ARTICLE OPEN ACCESS

Periodic Inverted Micropyramids for Optically Optimized Fully Textured Solution-Processed Perovskite Solar Cells

Hanifah Winarto[1] | Johannes Sutter[1] | Philipp Tockhorn[1] | Viktor Škorjanc[1] | Pramila Patil[1] | Sebastian Berwig[1] | Lea Zimmermann[1] | Guillermo Martínez-Denegri[1] | Steve Albrecht[1,2] | Christiane Becker[1,3]

[1]Solar Energy Division, Helmholtz-Zentrum Berlin für Materialien und Energie GmbH, Berlin, Germany | [2]Faculty of Electrical Engineering and Computer Science, Technical University Berlin, Berlin, Germany | [3]Hochschule für Technik und Wirtschaft Berlin, Berlin, Germany

Correspondence: Christiane Becker (christiane.becker@helmholtz-berlin.de)

Received: 6 August 2025 | **Revised:** 16 October 2025 | **Accepted:** 20 October 2025

Funding: European Innovation Council (EIC), Grant/Award Number: 101162377

Keywords: conformal coating | inverted pyramids | KOH etching | PbI_2 | perovskite solar cells | texture

ABSTRACT

Optical performance of perovskite-based solar cells can be enhanced by utilizing fully textured interfaces. However, solution processing of perovskite films on textured surfaces is a nonstraightforward and challenging process, particularly if optically most efficient micrometer-sized textures are used. In this work, we present fully textured solution-processed perovskite solar cells on periodic inverted micropyramids. The textures have a period of 4 μm with varying pyramid depths and are fabricated by wet-chemical etching of silicon with subsequent replication on glass substrates using nanoimprint lithography. Inverted pyramids are shown to enable low reflectance similar to random micropyramids on silicon. Additionally, they are able to confine perovskite precursor solution within its structure during spin coating, resulting in a conformal, fully textured perovskite film. We demonstrate that the resulting fully textured single-junction perovskite solar cells feature a reduced reflection loss of up to 1.2 mA/cm^2 in short-circuit current density. Moreover, we observe that the amount of lead iodide in the perovskite precursor solution crucially impacts growth and nonradiative recombination losses of the fully textured perovskite solar cells on inverted micropyramids. Finally, we prove the versatility of our approach by also demonstrating conformal coating with slot-die coating, which is a scalable process considered for industrial application.

1 | Introduction

Perovskite-based solar cells have been named the fastest growing solar technology, with increase in power conversion efficiency (PCE) from 3.8% in 2009 to 27.0% in 2025 [1]. For instance, efficiency of perovskite-silicon tandem solar cells has surpassed the detailed balance limit of efficiency for single-junction solar cells [2] with current record PCE at 34.85% [3]. Different approaches have been utilized to improve the performance of perovskite-based solar cells even further, with light management as a key strategy. Light management in a solar cell is done by extending the path length that light travels in the absorber, known as light trapping, and by minimizing reflectance at the front and interfaces between the layers to maximize the amount of light reaching the absorber [4]. Both light management methods can be achieved by utilizing textured interfaces within the solar cell. Implementation of textured interfaces in perovskite-silicon tandem solar cells has been integral to achieving past record efficiencies [5–9], and it continues to be an important pathway for further performance improvements. In conventional silicon solar cells, random pyramidal microtextures are commonly used and can be implemented by industrially compatible potassium hydroxide (KOH) etching of the silicon (100) surface [10]. Other micro- and nanotextures have also been implemented in silicon solar cells, such as inverted pyramids [11], black silicon [12], and sinusoidal textures [13]. Among the various textures

used for solar cells, inverted pyramidal textures, which can be manufactured by utilizing an etching mask on silicon during KOH etching, are discussed to have the potential to surpass the Lambertian limit of light trapping [14, 15].

When implementing textured interfaces in perovskite-based solar cells, the perovskite deposition method needs to be taken into account. Perovskite can be deposited through different approaches, such as solution- and vacuum-based processes, as well as hybrid deposition method [6, 8, 16, 17]. Without any modification within the processing method, perovskite deposition by solution processing on the commonly used random pyramidal microtexture would result in the pyramid tips being exposed above the perovskite layer, thus introducing shunts to the device. Depositing perovskite absorbers using solution-processing method on a textured interface is possible either through adjustment of the perovskite thickness or through modifications of the texture on the silicon surface, such as creating random pyramids with size smaller than the industrial standard [5, 18–20] and using nanostructures [13, 21, 22]. Smaller textures result in a textured interface between the substrate and perovskite absorber layer but a planar perovskite top interface, increasing reflection loss on the top surface. In contrast, optically preferable fully textured interfaces of the perovskite absorber layer in perovskite-silicon tandem solar cells were obtained by using vacuum-based and hybrid deposition processes [8, 17]. However, the performance of perovskite solar cells fabricated by vacuum-based deposition method are yet to achieve the same performance as solution-processed perovskites [23] but suffer from lower reproducibility when compared to solution processing [24].

Generally, light absorption in two-terminal monolithic perovskite-silicon tandem solar cell was found to be more effective for those with average texture size in micrometers [5, 7, 8, 25, 26] compared to their nanometer counterparts [9, 18–21]. Up to now, only a few studies have explored solution processing of perovskite on micrometer-sized textures. Recently, Ying et al. introduced a hierarchical nano–micropyramidal structure made on silicon through metal-assisted KOH etching. It was demonstrated that solution processing of perovskite on this texture results in fully textured interfaces in the perovskite-silicon tandem solar cell [26]. Turkay et al. demonstrated that protrusion-free perovskite films can be grown on random 2 μm micropyramids by solution processing by careful tailoring of the film thickness to match the pyramids' height profile [25]. Their hypothesis was that even if the pyramids' tip-to-base heights are greater than the perovskite thickness, the presence of small facet on the pyramid due to a "supporting" neighboring pyramid can enable full coverage.

In this study, we develop inverted pyramidal microtextures to enable conformal growth of solution-processed perovskite single-junction solar cells resulting in improved light management. The inverted pyramidal textures with different pyramid sizes are replicated on glass substrates using nanoimprint lithography (NIL) from etched silicon wafers. These glasses are utilized as textured substrates for perovskite single-junction solar cells. We show that perovskite deposition by solution processing on the periodic inverted pyramids results in a near-conformal growth of fully textured perovskite layer, yielding in a higher short-circuit current density (J_{SC}) compared to its planar counterparts. The fully textured interface of the perovskite film is achieved without adaptation of the precursor solution and spin coating parameters. Beyond that, the content of lead iodide (PbI_2) in the precursor solution is found to be critical in the textured perovskite solar cells to achieve comparable open circuit voltage (V_{OC}) to their planar counterparts.

2 | Results

2.1 | Periodic Inverted Pyramids with Different Pyramid Sizes

A preliminary experiment was done on sinusoidal textures to observe how perovskite films with varying thickness form on textures, which is shown in Section S1 on the Supporting Information. These preliminary experiments indicated that the ratio of perovskite layer thickness, as a result of perovskite precursor solution concentration, and texture period is a crucial parameter on the perovskite film growth on textured surfaces. It was observed that an approximately 90-nm-thick perovskite can grow conformally on texture with period of 750 nm. By using this ratio of 1:8 for perovskite absorber thickness by texture periodicity, a texture period of 4 μm was selected with the goal of accommodating conformal growth of approximately 500-nm-thick perovskite on textures. This texture size was also selected by considering that to date, microscale textures yielded better optical performance than nanoscale textures. Periodic inverted micropyramids were selected due to the possibility to adjust texture height while keeping the periodicity constant.

Various inverted pyramid sizes with same periodicity of 4 μm were first fabricated by modifying the KOH etching duration of (100) oriented silicon wafers and the opening size of the silicon oxide etching mask. The schematic illustration of the fabrication process of the inverted pyramids can be seen in Figure 1. Periodic inverted pyramids can be obtained on (100) oriented silicon wafers by KOH etching with an etching mask with periodic openings. As shown in Figure 1a, due to the different etching rates of different planes of silicon crystal lattice, where (100) plane is etched faster than (111) plane, the KOH etching results in grooves with angle of 54.7° within the openings of the etching mask, creating periodic inverted pyramids. This structure can be transferred onto glass by NIL, as shown in Figure 1b, by utilizing a UV-curable photoresist with refractive index similar to that of glass. This allows for perovskite single-junction solar cell fabrication on inverted pyramids using glass substrates with reproducible texture sizes. As shown in the scanning electron microscopy (SEM) images in Figure 1c, different inverted pyramid sizes on silicon represented by their structure depth were obtained from different etching duration and mask opening size. With longer etching duration, larger pyramids beyond the size of the etching mask opening can be obtained. To create smaller pyramids, an etching mask with smaller opening size is utilized.

The reflectance of the etched silicon substrates with periodic inverted pyramids were measured by optical UV/Vis spectrophotometry, followed by calculation of short-circuit current density loss caused by the reflectance (J_R) by weighing the

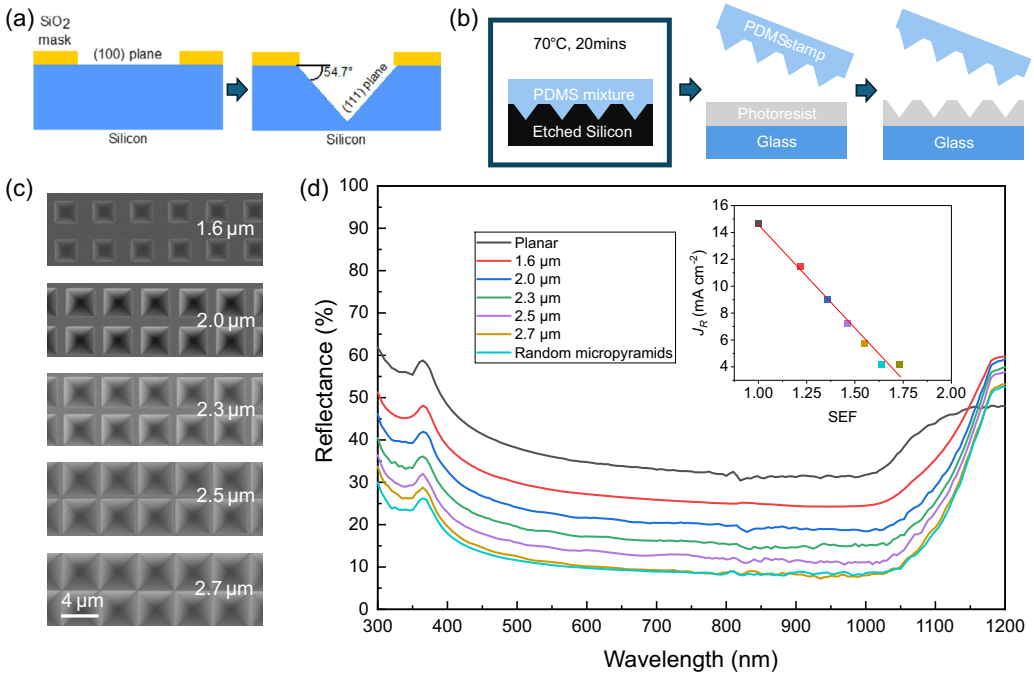

FIGURE 1 | Fabrication and replication of periodic inverted pyramidal microtextures. (a) Illustration of the KOH etching mechanism of silicon with an SiO_2 etching mask. (b) The inverted pyramidal structure on silicon is replicated on glass by using NIL, where the structure is copied using a PDMS stamp and transferred onto glass substrate by using a UV-curable photoresist with refractive index similar to that of glass. (c) SEM images of the etched silicon with pyramid depths of 1.6, 2.0, 2.3, 2.5, and 2.7 µm. Scale bar is valid for all SEM images in this figure. (d) The reflectance spectra (R) of silicon samples textured with periodic inverted pyramids with various pyramid depths compared with a planar interface and random pyramids. Comparison of current density loss equivalent of R based on AM1.5G (J_R) for each texture and their respective surface enhancement factor (SEF) is shown as an inset in the reflectance plot.

resulting reflectance spectra from 300 to 1200 nm with the AM1.5G solar spectrum at each wavelength as a figure of merit. Comparison of the performance of each pyramid sizes with their planar and random pyramidal benchmarks was done using J_R and their respective surface enhancement factor (SEF). The resulting reflectance spectra, along with their respective J_R, can be seen in Figure 1d.

From the comparison of the reflectance spectra for each texture and their respective J_R shown in Figure 1d, it is evident that both reflectance and J_R decrease with larger inverted pyramid size and that the largest inverted pyramid size (around 2.7 µm deep) has a reflectance spectrum similar to that of silicon with random micropyramidal texture. Lower reflectance and J_R for larger pyramid size occurs due to the enhanced light in-coupling and light trapping of the textures [27]. On the contrary, a smaller pyramid size features larger flat area on the surface of the sample, which contributes to the higher reflectance and thus higher J_R. The extent to which presence of larger flat area on the surface might assist perovskite deposition and growth by solution processing on a textured substrate has to be investigated.

From these considerations, textures with pyramid depths of 1.6, 2.0, and 2.3 µm are then selected for further perovskite single-junction solar cell investigation. The investigation aims to understand how the perovskite layer forms on periodic inverted pyramids and how this influences the solar cell device performance. The textures were then transferred from the etched silicon onto glass substrates by NIL, as shown in Figure 1b. The glass substrates with the transferred inverted pyramidal structure were then coated with indium tin oxide (ITO) in the next step and used as the substrate for the fabrication of perovskite single-junction solar cells.

2.2 | Perovskite Solar Cells on Periodic Inverted Pyramids

$Cs_{0.05}(MA_{0.23}FA_{0.77})_{0.95}Pb(I_{0.77}Br_{0.23})_3$ (triple cation) perovskite absorber aimed for the bandgap of 1.68 eV was deposited by spin coating on glass substrates with periodic inverted pyramids coated with ITO and 2PACz self-assembled monolayer, without modifying any spin coating parameters from their planar counterpart. The perovskite spin-coated on the inverted pyramids grows almost conformally following the hills and valleys of the pyramids, which are shown on the SEM cross-section images in Figure 2a–d. Inverted micropyramidal texture can accommodate conformal growth of perovskite due to its confining nature, which may allow perovskite precursor solutions with the optimum concentration to stay within the valleys of the texture during processing.

The perovskite deposited on different pyramid sizes features different average apparent domain sizes, which can be observed from the top-view SEM images in Figure 2e–h. To quantify the domain size analysis, perovskite domain sizes within 10 µm^2 area of the SEM images were measured for the perovskite samples on planar and on 2.0 µm deep inverted pyramids, and the result is shown in Figure 2i. The perovskite deposited on inverted pyramids show larger domain sizes with average grain size of 0.08 µm^2, compared to its planar counterpart with average

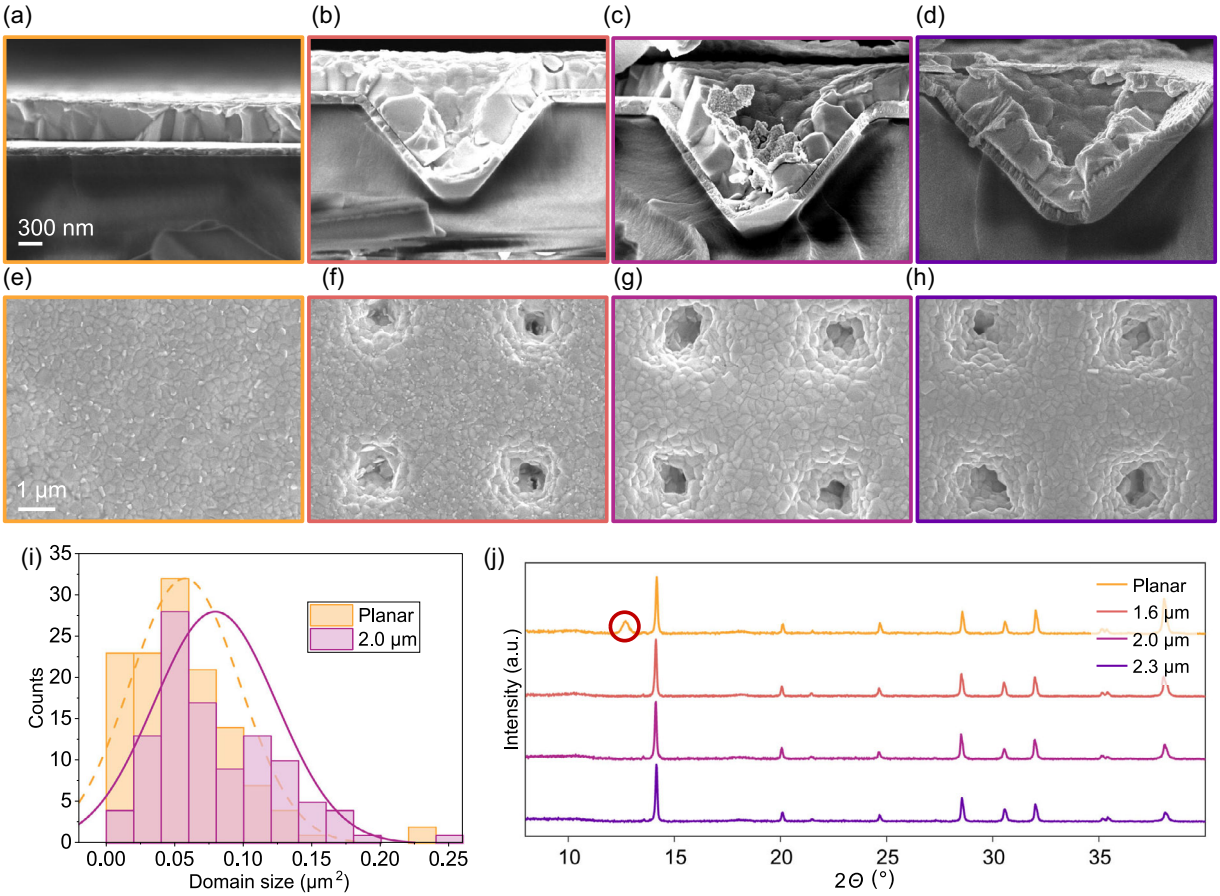

FIGURE 2 | Structure analysis of the fully textured perovskite. SEM images of perovskite layer deposited on (a,e) planar and (b–d,f–h) textured substrates with inverted pyramidal textures, with pyramid depths of (b,f) 1.6 µm, (c,g) 2.0 µm, and (d,h) 2.3 µm, viewed from (a–d) cross-section and from (e–h) top view. The scale bar applies to all SEM images in the same row. (i) Domain size distribution of perovskite film on planar and 2.0 µm deep inverted pyramids. (j) Normalized XRD diffractograms of perovskite layers deposited on planar and textured substrates with PbI_2 (001) diffraction peak marked with red circle.

domain size of 0.06 µm^2. Larger domains have been reported to be beneficial for charge transfer between the perovskite and the charge transport layers [28] as domain boundaries were identified as bottlenecks for charge transfer [29]. The appearance of bright flakes, with size smaller than the perovskite domains, can be observed on the perovskite deposited on planar as well as on 1.6 µm inverted pyramids, but not on 2.0 and 2.3 µm inverted pyramids. These bright flakes likely originate from PbI_2, which has been observed in halide perovskites employing excess PbI_2 content in the precursors [30, 31].

To further investigate these bright flakes and understand the difference in surface chemistry between perovskite grown on planar and inverted pyramids, X-ray diffraction (XRD) measurements are conducted. From the resulting XRD diffractogram shown in Figure 2j, it is apparent that the perovskite on planar substrate features a PbI_2 (001) peak at 12.7°, while this is not visible for the perovskite deposited on all samples with inverted pyramids. As previously reported, PbI_2 may assist in passivating the perovskite surface [32, 33] affecting the energy level alignment of the interface between the perovskite and electron transport layer (ETL).

This difference in PbI_2 peak in the XRD diffractograms was not observed in our previous publication regarding perovskite on nanotextures [22]. Notably, Farag et al. reported on less PbI_2 on perovskite surface when employing random upward pyramidal textured surface with average pyramid heights of 1–2 µm [34]. This may indicate that textured substrates, especially with texture size in the micrometer range, may alter the perovskite crystallization process.

Since the texture studied in this research presents a considerable portion of flat areas that resembles the planar sample, we characterized the cross section of perovskite samples on planar and 2.0 µm deep inverted pyramids using energy-dispersive X-ray spectrometry (EDX) with the results presented in Figure S2. The EDX spectra in Figure S2c show a similar relative signal contribution from each of the elements contained in the perovskite layer. This result, together with the difference on crystalline PbI_2 found in the XRD characterization, suggests a different perovskite growth trend. While PbI_2 crystallizes during the growth of perovskite film in the planar sample, the excess of this compound in the solution might be dispersed within the perovskite lattice without crystallizing in the textured samples. Moreover, we also compared the EDX spectra of different areas in the perovskite layer grown on the textured sample. Figure S2d shows the results from the EDX measurement on the flat top area of perovskite on the inverted pyramidal textures (hills) and the bottom

part of the inverted pyramids (valleys). In this case, different perovskite compositions are observed if one considers the ratio of the most intense Br and Pb lines (1.48 and 2.35 keV, respectively). Such results suggest some type of segregation affected by the geometry of the substrate. However, the explanation for these structural and compositional differences lays beyond the scope of this study and requires a more thorough analysis.

Perovskite single-junction solar cells were fabricated by depositing fullerene (C_{60}) and bathocuproine (BCP) as ETL and buffer layer, respectively, as well as silver rear electrodes on the perovskite layer with the above shown periodic inverted pyramidal textures. The performance characterization results of the fabricated solar cells are shown in Figure 3. From the current density–voltage (J–V) and external quantum efficiency (EQE) of the best-performing solar cells from each texture category shown in Figure 3a,b, it is apparent that the perovskite solar cells deposited on the 2.3 µm deep inverted pyramids are able to achieve the highest J_{SC} of 20.8 mA/cm^2 compared to perovskite deposited on planar and smaller inverted pyramids sizes. The reflectance of planar samples calculated to J_R of 2.76 mA/cm^2 in the range 300–750 nm decreases to 1.71 mA/cm^2 for fully textured perovskite solar cells with 2.3 µm deep inverted pyramids. This translates to an increase in J_{SC} of the solar cells up to 1.2 mA/cm^2. Moreover, the J_{SC} of the solar cells increases with increasing pyramid size, in agreement with the decrease in J_R calculated from the reflectance of each solar cell shown in Figure 3b next to the legend. This overall decrease in reflectance and J_R might be attributed to improved light trapping by double bounce effect, where reflected light can be directed back to the perovskite since the angle of the texture at the substrate-perovskite interface is larger than 45°. Although all textures in this study feature the same angle of 54.7°, the difference in optical performances of the different texture sizes is most probably caused by the share of planar area between the inverted pyramids, with the 2.3 µm deep inverted pyramids having the smallest planar area.

On the contrary, the V_{OC} of the solar cells decreases with increasing pyramids size, with 2.3 µm deep inverted pyramids featuring the lowest V_{OC}. This trend, where the V_{OC} and thus efficiency decrease with increasing pyramid size, can also be seen in the statistics of the performance parameters of the solar cells throughout 30 cells made with the same fabrication procedure for each texture shown in Figure S3a–d. As shown in Figure S3a–d, the performance of perovskite solar cells fabricated on large pyramids has a larger spread in most of the performance parameters compared to samples with other pyramid sizes, indicating a large variation despite being fabricated with the same method and from the same precursor solution as other solar cells on smaller pyramid sizes. To understand this difference in performance, especially in the V_{OC}, absolute photoluminescence (PL) measurements were performed, and quasi-Fermi-level

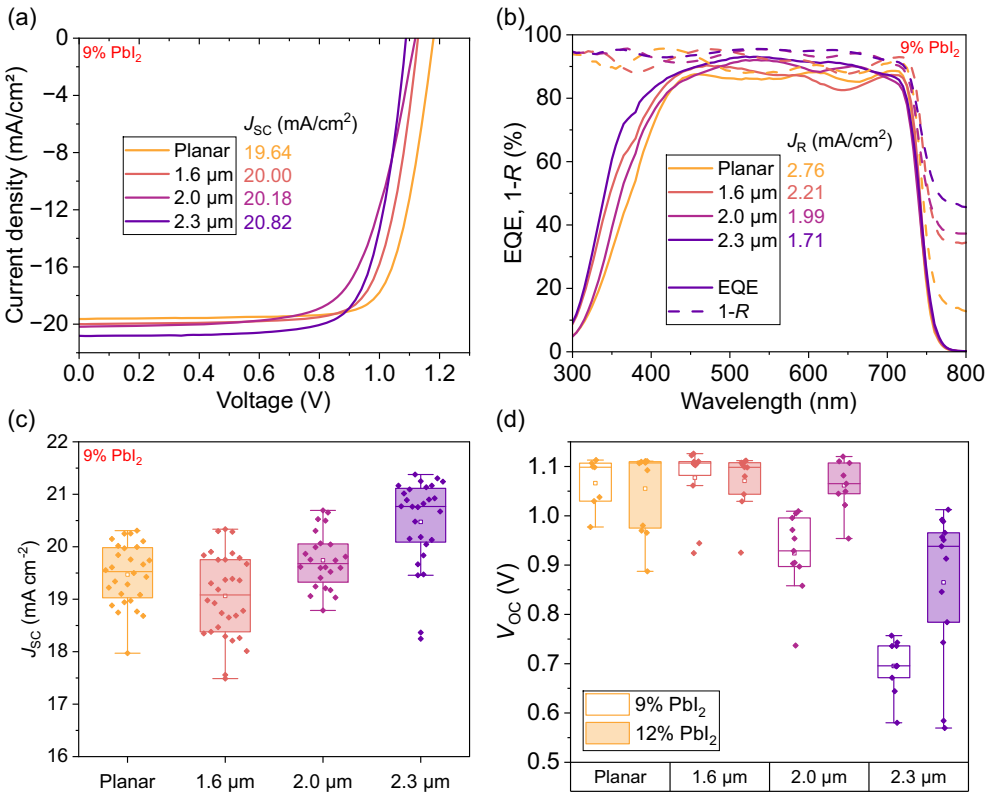

FIGURE 3 | Performance of perovskite solar cells fabricated on inverted pyramidal microtextured surfaces. (a) J–V characterization and (b) EQE with 1-Reflectance of the perovskite solar cells fabricated on inverted pyramidal textures compared to planar. The J–V curve was adjusted with the integrated J_{SC} obtained from EQE measurements. J_R as a measure of reflectance losses is shown next to the legend in the EQE graph for each sample. (c) J_{SC} distribution of the perovskite solar cells on inverted micropyramidal textures and planar substrates, fabricated with the same procedure and grouped by pyramid size. (d) V_{OC} of perovskite solar cells fabricated with different excess PbI_2 content from another deposition run, grouped by pyramid size.

splitting (QFLS) were calculated. The resulting PL spectra of the representative solar cells are shown in Figure S3e, with their respective QFLS displayed in Figure S3f.

As shown in Figure S3e, the PL peaks of the perovskite solar cells shifted toward longer wavelength for larger texture size, with perovskites on 2.0 and 2.3 μm deep inverted pyramids having similar PL peak positions. On one hand, this shift in PL peak position for textured solar cells was also observed in [22, 35, 36] and can be attributed to optically enhanced PL emission for photons with longer wavelength due to texture [37]. On the other hand, the PL peak position of the planar perovskite solar cell lies on a shorter wavelength, which correlates to the appearance of PbI_2 detected by the XRD diffractograms on the planar sample shown on Figure 2i, where excess PbI_2 results in the increase of the bandgap of perovskite [38].

From the absolute PL spectra in Figure S3e, the QFLS was calculated by high-energy tail fit method [39, 40]. The resulting QFLS of the full-stack perovskite solar cell shown in Figure S3f showed that perovskite deposited on larger texture has slightly lower QFLS and a higher mismatch between V_{OC} and QFLS of up to 40 mV for the 2.3 mm deep inverted pyramids. This may indicate an increase in nonradiative recombination in the solar cell [41] for the larger pyramids size. This can also be attributed to the lack of PbI_2 detected on the samples with textures from the XRD diffractograms shown in Figure 2i, since PbI_2 is able to suppress nonradiative recombination [42]. It was also observed that textures in solar cells have a larger influence on the PL spectral intensity when compared to improved electronic quality of the absorber [36]. Textures are able to improve the out-coupling of light, thus increasing the value of QFLS [22].

As previously discussed within this chapter, utilization of textured substrates may alter the crystallization process of perovskite, leading to differences in surface morphology or cell performance. Other than the difference in domain size distribution and in the amount of PbI_2 detected on the surface of perovskite, the perovskite solar cells deposited on this texture also have lower V_{OC} compared to their planar counterpart. To account for the PbI_2 deficiency on perovskite deposited on inverted pyramidal textures and evaluate their performance, we devised an experiment with purposely adding excess lead iodide into the perovskite precursor solution, which is described in detail in Section S5 of the Supporting Information.

From the results discussed in Section S5, further experiment regarding device fabrication using excess PbI_2 content of 12% was done in comparison with the default excess PbI_2 content of 9%. As shown in Figure 3d, 12% of excess PbI_2 content is able to lift the V_{OC} of the textured perovskite solar cells, with the V_{OC} of perovskite solar cells with 1.6 and 2.0 μm deep pyramids being on par with their planar counterpart. While the J_{SC} of the solar cells with different excess PbI_2 contents are comparable, as shown on Figure S6a, improvements in V_{OC} and fill factor (FF) (Figure S6b) affect the PCE of the textured solar cells positively, which can be seen in Figure S6c.

To understand if this increase in performance is due to the appearance of PbI_2 flakes, XRD measurements were done on the samples prepared from the precursor solution with 12% excess PbI_2 content. From the XRD diffractograms shown in Figure S7, the peak for PbI_2 (001) can only be detected on the planar sample, similar to the solar cells fabricated with the default 9% excess PbI_2 content as shown in Figure 2j but with higher intensity. This conflicts with the results shown in Figure S5e,f, where a small amount of bright flakes can be seen on the SEM images of perovskite with 12% and 15% excess PbI_2. Therefore, the bright flakes in Figure S5e,f might possibly be attributed to noncrystalline PbI_2 or a different perovskite phase. It can also imply that the amount of PbI_2 on the surface is below the detection threshold of XRD. Although the appearance of PbI_2 crystals could not be detected by XRD, the increase in V_{OC} and efficiency of the fresh devices can be attributed to the excess amount of PbI_2 in the precursor solution, which may contribute in reducing defect concentration on the solar cells by shifting the reaction equilibrium of the crystallization of the perovskite absorber [43].

We note that the use of excess PbI_2 for improved passivation is controversial, since it may reduce device stability due to the decomposition of PbI_2 into Pb^0 and I_2 under illumination [44, 45]. The effect of excess PbI_2 in perovskite precursor or its appearance as domains on perovskite absorber layer has been widely discussed within the community [30, 43, 45–48] and was observed to impact the performance of perovskite solar cells both positively and negatively. Nonetheless, we use excess PbI_2 in perovskite precursor as a model system to demonstrate the necessity of tailoring deposition processes for textured substrates to achieve comparable device performances.

2.3 | Fully Textured Perovskite Absorber on Inverted Pyramids From Slot-Die Coating

To demonstrate the upscalability of the fully textured perovskite layers deposited on inverted pyramidal textures, a proof-of-concept experiment with slot-die coating of perovskite absorber on substrates with 1.6 and 2.3 μm deep inverted pyramids were conducted. In this experiment, $MA_{0.6}FA_{0.4}PbI_3$ perovskite with bandgap of 1.56 eV is utilized instead of triple cation perovskite. The resulting SEM image of the slot-die coated perovskite on planar and inverted pyramids can be seen in Figure 4. From the tilted SEM images in Figure 4b,c, we can clearly see that perovskite can also be deposited almost conformally on the inverted pyramids using slot-die coating, which enables an alternative up-scaling method of perovskite-based solar cells with improved optics from the fully textured interface.

To quantify the optical performance of the slot-die coated perovskite absorbers, reflectance measurement and J_R calculation for the wavelength range of 300–800 nm were done on the samples. The reflectance spectra and J_R calculation results, which can be seen in Figure 4d, indicate that the fully textured slot-die coated perovskite films also exhibit improved light trapping compared to its planar counterpart. Moreover, by using $MA_{0.6}FA_{0.4}PbI_3$ in this experiment instead of triple cation perovskite, it is also proven that conformal growth of perovskite on inverted pyramids can be done to reduce reflection of different perovskite compositions.

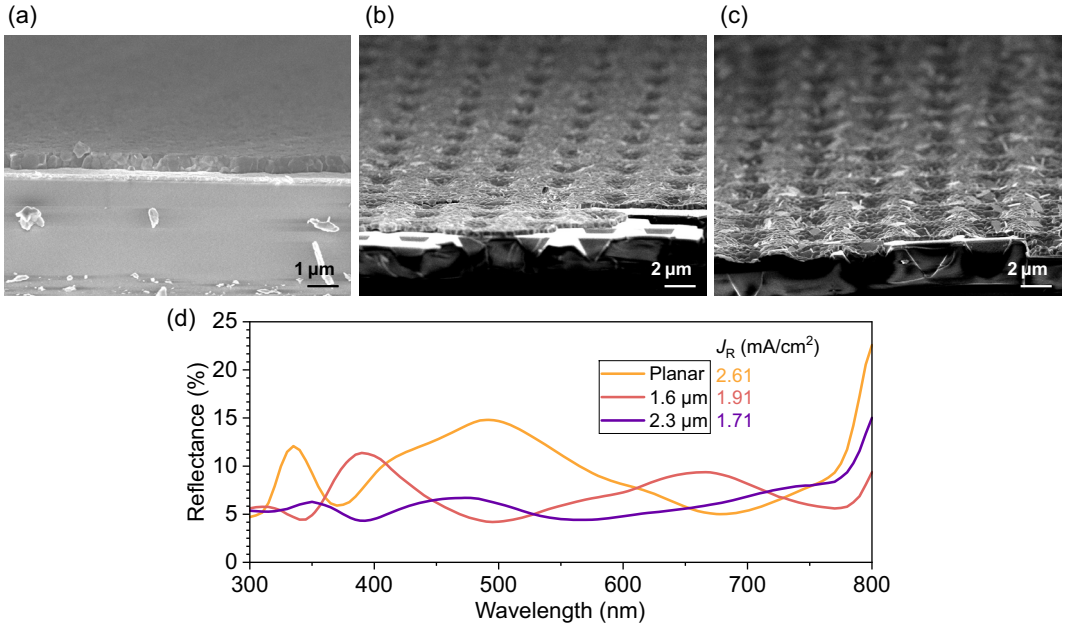

FIGURE 4 | Perovskite absorber layer deposited on inverted pyramids using slot-die coating. Tilted top-view SEM images of perovskite absorber layer deposited with slot-die coating on (a) planar substrate along with (b) 1.6 and (c) 2.3 µm deep inverted pyramids on glass substrate. (d) Reflectance spectra of the slot-die coated perovskite absorber on planar and textured substrates. J_R calculation result as a measure of reflectance losses are shown next to the legend.

3 | Conclusion

Inverted pyramidal textures with a structure period of 4 µm and different pyramid depths were developed by wet-chemical etching process of silicon, resulting in textures with low reflectance comparable to that of random micropyramids. The textures, optimized to accommodate a conformal growth of 500-nm-thick perovskite absorber, were utilized for the fabrication of fully textured single-junction perovskite solar cells using spin coating. We demonstrated that the fully textured solution processed perovskite solar cells feature an increase of up to 0.5 mA/cm^2 in short-circuit current density due to reduced reflection losses. We also found that the growth of perovskite layers on inverted micropyramids may require tailoring in the fabrication process as a comparable V_{OC} and FF to their planar counterpart was achieved upon utilizing surplus excess PbI_2 in the perovskite precursor solution. Moreover, we showed that fully textured perovskite absorber layer can be deposited on the inverted micropyramidal textures using slot-die coating. These findings demonstrate that fully textured perovskite solar cells can be fabricated on microscale textured surfaces with solution processing, enabling further development of upscalable, optically optimized perovskite-silicon tandem solar cells.

4 | Methods

4.1 | Texture Fabrication

The periodic inverted pyramidal template textures were fabricated through wet chemical etching of silicon with a patterned SiO_2 etching mask. To create the etching mask, 250 nm of SiO_2 was deposited on silicon, and photolithography was used to transfer the 4 µm periodic pattern before going through reactive ion etching process. The wet chemical etching process of the silicon was then done in 5 wt% KOH solution at 83°C with CellTex Ultra as an additive. Etching duration was determined from trials, starting from when the pyramids start to form up until the etching mask starts to deteriorate, in 2-min increment. Longer KOH etching times create an undercut below the etching mask, creating larger pyramids. The maximum inverted pyramid size that would be achieved when the sides of the pyramid created within one etching mask opening almost touches the pyramids created within the mask opening next to it. Since the smallest inverted pyramid size that can be obtained during KOH etching would be the size of the opening of the etching mask, a smaller opening size is needed to create smaller pyramids. Modification of the opening size of the etching mask was done by utilizing a UV dose higher than the standard recipe for the photoresist used in the photolithography process. As a reference, a silicon wafer without SiO_2 mask was etched for 8 min to obtain a random pyramidal texture. The resulting texture was transferred onto 2.5×2.5 cm^2 glass substrates from Corning Eagle by NIL process to produce the textured substrates for the fully textured single junction silicon solar cell.

4.2 | Perovskite Solar Cell Fabrication

One hundred fifty nanometers of indium tin oxide (ITO) as the front electrode was sputtered onto the textured glass substrates and immediately annealed at 200°C for 10 min. The substrates were then processed in a glovebox filled with nitrogen. For the hole transport layer, 100 µL of 2PACz (from TCI) solution in ethanol with 1 mM concentration was deposited by spin coating and annealed at 100°C for 7 min. The $Cs_{0.05}(MA_{0.23}FA_{0.77})_{0.95}Pb(I_{0.77}Br_{0.23})_3$ perovskite absorber, aimed for the bandgap of 1.68 eV, was made by adapting the recipe

from [49]. The precursor solutions were prepared by combining a mixture of formamidinium iodide (FAI) from Dyenamo and lead iodide (PbI_2) from TCI with a mixture of methylammonium bromide (MABr) from Dyenamo and lead bromide ($PbBr_2$) from TCI in a ratio of 77:23. Both precursor solutions were dissolved in a mixture of anhydrous dimethylformamide (DMF) and dimethylsulfoxide (DMSO) from Sigma–Aldrich in a volume ratio of DMF:DMSO 4:1 and consist of 1 M of the organics and 1.1 M of the lead salts. 5%vol cesium iodide (CsI) from abcr with concentration of 1.5 M in DMSO was added to the precursor solutions. The spin coating of the precursor solution was done for 40 s in 3500 rpm, and 32 s after the start of the spin coating 400 µL of Anisole from Sigma–Aldrich was poured as antisolvent. The films were then annealed for 20–30 min at 100°C. For the ETL, 23 nm of C_{60} (Sigma–Aldrich) and 8 nm of Bathocuproine (Sigma–Aldrich) as buffer were deposited through evaporation at 1×10^{-6} mbar, followed by evaporation of 100 nm of Ag as the back electrode. All evaporation processes done on textured samples were adjusted with SEF of 1.3 to accommodate the increase in surface area due to the textured interface [50].

4.3 | Slot-Die Coating of Perovskite Absorber Layer

1.27 M of $MA_{0.6}FA_{0.4}PbI_3$ perovskite precursor solution was prepared with acetonitrile (ACN), 2-methoxyethanol (2-ME), and N-methyl-2-pyrrolidone (NMP) in a volume ratio of ACN: 2-ME:NMP 23:23:4 and deposited on the glass/resist/ITO/Me-4PACz stack using slot-die coating with coating speed of 30 cm/s. The films were moved through an air knife and annealed at 125°C for 15–20 min.

4.4 | Characterizations

SEM was performed using Zeiss MERLIN Field Emission SEM with a GEMINI II optical column. Domain size measurement and distribution analysis were done using ImageJ software by manually marking each perovskite grain in the SEM image at the grain boundaries. XRD diffractograms were measured in Bragg–Brentano geometry with Bruker D8 diffractometer using Cu K-alpha radiation from an X-ray tube operated at 40 mA and 40 kV acceleration voltage, where step size of 0.02 2θ and integration time of 0.8 s were used. Atomic force microscopy (AFM) measurements were performed with XE-70 AFM by Park Systems, featuring a nanoscopic high aspect ratio tip. Lambda-1050 UV/Vis/NIR Spectrophotometer from PerkinElmer was used to measure reflectance from 300 to 800 nm with 5 nm steps and a tilting angle of 8°. *J–V* characterization was done using Keithley 2400 source-measure unit and Oriel LCS-100 solar simulator, mimicking 1000 W/m^2 of AM1.5G spectrum (calibrated to a reference of filtered KG-3 silicon solar cell). Shadowing mask with opening size of 0.09 cm^2 to define the active area is always used during the *J–V* measurement. EQE was measured using QE-R Quantum Efficiency System from Enlitech with a Xenon lamp and a monochromator. Absolute PL measurement was done with QuantY Pro from Quantum Yield Berlin using 532 nm laser with spot size of 0.12 cm^2 and photon flux of 1.2×10^{16} photons/s.

Acknowledgments

The authors would like to thank I. Rudolph for the technical support in BESSY II clean room; K. Jacob for the support in Energy Materials In-situ Laboratory Berlin (EMIL) cleanroom; F. Riesebeck for nanoimprint lithography and ITO deposition; F. Ruske for supporting the cross section EDX measurements; and J. Beckedahl, C. Ferber, M. Choyne, and H. Heinz for the technical support in HySPRINT Photovoltaics Lab. The Energy Materials In-situ Laboratory Berlin (EMIL) operated by the Helmholtz-Zentrum für Materialien und Energie GmbH (HZB) is acknowledged for granting access to its sample characterization laboratory. G.M.-D. received funding from the European Innovation Council (EIC) under grant agreement No. 101162377 in the framework of the European project JUMP-INTO-SPACE.

Open Access funding enabled and organized by Projekt DEAL.

Conflicts of Interest

The authors declare no conflicts of interest.

Data Availability Statement

The data that support the findings of this study are available from the corresponding author upon reasonable request.

References

1. Best Research-Cell Efficiency Chart | Photovoltaic Research | NREL. Accessed: October 31, 2025. https://www.nrel.gov/pv/cel-lefficiency.

2. W. Shockley and H. J. Queisser, "Detailed Balance Limit of Efficiency of p-n Junction Solar Cells," *Journal of Applied Physics* 32, no. 3 (1961): 510–519, https://doi.org/10.1063/1.1736034.

3. E. Bellini and V. Shaw, "Longi Achieves 34.85% Efficiency for Two-Terminal Tandem Perovskite Solar Cell," *pv magazine International*. Accessed October 31, 2025. https://www.pv-magazine.com/2025/04/18/longi-achieves-34-85-efficiency-for-two-terminal-tandem-perovskite-solar-cell/.

4. R. Vismara, "Advanced Light Management in Thin-Film Solar Cells" (*PhD thesis*, Technische Universiteit Delft, 2020), https://doi.org/10.4233/uuid:f3f07a75-223a-43be-9da4-d063bee67f56.

5. J. Liu, Y. He, L. Ding, et al., "Perovskite/Silicon Tandem Solar Cells with Bilayer Interface Passivation," *Nature* 635, no. 8039 (Sept. 2024): 596–603, https://doi.org/10.1038/s41586-024-07997-7.

6. E. Ugur, A. A. Said, P. Dally, et al., "Enhanced Cation Interaction in Perovskites for Efficient Tandem Solar Cells with Silicon," *Science* 385, no. 6708 (Aug. 2024): 533–538, https://doi.org/10.1126/science.adp1621.

7. E. Aydin, E. Ugur, B. K. Yildirim, et al., "Enhanced Optoelectronic Coupling for Perovskite/Silicon Tandem Solar Cells," *Nature* 623, no. 7988 (Nov. 2023): 732–738, https://doi.org/10.1038/s41586-023-06667-4.

8. X. Y. Chin, D. Turkay, J. A. Steele, et al., "Interface Passivation for 31.25%-Efficient Perovskite/Silicon Tandem Solar Cells," *Science* 381, no. 6653 (Jul. 2023): 59–63, https://doi.org/10.1126/science.adg0091.

9. P. Tockhorn, J. Sutter, A. Cruz, et al., "Nano-Optical Designs for High-Efficiency Monolithic Perovskite–silicon Tandem Solar Cells," *Nature Nanotechnology* 17, no. 11 (Nov. 2022): 1214–1221, https://doi.org/10.1038/s41565-022-01228-8.

10. G. T. A. Kovacs, N. I. Maluf, and K. E. Petersen, "Bulk Micromachining of Silicon," *Proceedings IEEE* 86, no. 8 (1998): 1536–1551, https://doi.org/10.1109/5.704259.

11. A. Razzaq, V. Depauw, H. S. Radhakrishnan, et al., "Infrared Absorption Enhancement Using Periodic Inverse Nanopyramids in Crystalline-Silicon Bottom Cells for Application in Tandem Devices,"

IEEE Journal of Photovoltaics 10, no. 3 (May 2020): 740–748, https://doi.org/10.1109/JPHOTOV.2020.2972324.

12. H. Savin, P. Repo, G. Von Gastrow, et al., "Black Silicon Solar Cells with Interdigitated Back-Contacts achieve 22.1% Efficiency," *Nature Nanotechnology* 10, no. 7 (Jul. 2015): 624–628, https://doi.org/10.1038/nnano.2015.89.

13. J. Sutter, D. Eisenhauer, P. Wagner, et al., "Tailored Nanostructures for Light Management in Silicon Heterojunction Solar Cells," *Solar RRL* 4, no. 12 (Dec. 2020):https://doi.org/10.1002/solr.202000484.

14. S. Bhattacharya and S. John, "Beyond 30% Conversion Efficiency in Silicon Solar Cells: A Numerical Demonstration," *Scientific Reports* 9, no. 1 (Aug. 2019): 12482, https://doi.org/10.1038/s41598-019-48981-w.

15. M. A. Green and Z. Zhou, "Light-Trapping by Wave Interference in Intermediate-Thickness Silicon Solar Cells": Comment," *Optical Express*,33, no.18 (Sept. 2025):https://doi.org/10.1364/OE.546086.

16. S. Mariotti, E. Köhnen, F. Scheler, et al., "Interface Engineering for High-Performance, Triple-Halide Perovskite–silicon Tandem Solar Cells," *Science* 381, no. 6653 (Jul. 2023): 63–69, https://doi.org/10.1126/science.adf5872.

17. M. Roß, S. Severin, M. B. Stutz, et al., "Co-Evaporated Formamidinium Lead Iodide Based Perovskites with 1000 hr Constant Stability for Fully Textured Monolithic Perovskite/Silicon Tandem Solar Cells"," *Advanced Energy Material* 11, no. 35 (Sept. 2021): https://doi.org/10.1002/aenm.202101460.

18. M. De Bastiani, R. Jalmood, J. Liu, et al., Monolithic Perovskite/Silicon Tandems with >28% Efficiency: Role of Silicon-Surface Texture on Perovskite Properties," *Advanced Function Material*, 33, no. 4 (Jan. 2023): https://doi.org/10.1002/adfm.202205557.

19. A. Harter, S. Mariotti, L. Korte, R. Schlatmann, S. Albrecht, and B. Stannowski, "Double-Sided Nano-Textured Surfaces for Industry Compatible High-Performance Silicon Heterojunction and Perovskite/Silicon Tandem Solar Cells," *Progress in Photovoltaics: Research and Applications* 31, no. 8 (Aug. 2023): 813–823, https://doi.org/10.1002/pip.3685.

20. Y. Li, H. Sai, C. McDonald, et al., "Nanoscale Size Control of Si Pyramid Texture for Perovskite/Si Tandem Solar Cells Enabling Solution-Based Perovskite Top-Cell Fabrication and Improved Si Bottom-Cell Response," *Advanced Materials Interfaces* (Sept. 2023): 2300504, https://doi.org/10.1002/admi.202300504.

21. Z. Ying, Z. Yang, J. Zheng, et al., "Monolithic Perovskite/Black-Silicon Tandems Based on Tunnel Oxide Passivated Contacts," *Joule* 6, no. 11 (Nov. 2022): 2644–2661, https://doi.org/10.1016/j.joule.2022.09.006.

22. P. Tockhorn, J. Sutter, R. Colom, et al., "Improved Quantum Efficiency by Advanced Light Management in Nanotextured Solution-Processed Perovskite Solar Cells," *ACS Photonics* 7, no. 9 (Sept. 2020): 2589–2600, https://doi.org/10.1021/acsphotonics.0c00935.

23. T. Abzieher, T. Feeney, F. Schackmar, et al., "From Groundwork to Efficient Solar Cells: On the Importance of the Substrate Material in Co-Evaporated Perovskite Solar Cells," *Advanced Function Material*, 31, no. 42 (Oct. 2021): https://doi.org/10.1002/adfm.202104482.

24. Y. Vaynzof, The Future of Perovskite Photovoltaics—Thermal Evaporation or Solution Processing?," *Advanced Energy Material*, 10, no. 48 (Dec. 2020): https://doi.org/10.1002/aenm.202003073.

25. D. Turkay, K. Artuk, M. Othman, et al., "Beyond Flat: Undulated Perovskite Solar Cells on Microscale Si Pyramids by Solution Processing," *ACS Energy Letters* 10 (Feb. 2025): 1397–1403, https://doi.org/10.1021/acsenergylett.5c00221.

26. Z. Ying, X. Guo, H. Du, et al., "Hierarchical Micro/Nanostructured Perovskite/Silicon Tandem Solar Cells with Fully Textured Solution-Processed Conformal Perovskite Absorbers," *ACS Energy Letters* 9 (Jul. 2024): 4018–4023, https://doi.org/10.1021/acsenergylett.4c01594.

27. S. Eyderman, S. John, M. Hafez, et al., "Light-Trapping Optimization in Wet-Etched Silicon Photonic Crystal Solar Cells," *Journal of Applied Physics* 118, no. 2 (Jul. 2015): 023103, https://doi.org/10.1063/1.4926548.

28. X. Zhao, Z. Wang, W. Tian, et al., "A Positive Correlation between Local Photocurrent and Grain Size in a Perovskite Solar Cell," *Journal of Energy Chemistry* 72 (Sept. 2022): 8–13, https://doi.org/10.1016/j.jechem.2022.04.033.

29. C. Cho, S. Feldmann, K. M. Yeom, et al., "Efficient Vertical Charge Transport in Polycrystalline Halide Perovskites Revealed by Four-Dimensional Tracking of Charge Carriers," *Nature Materials* 21, no. 12 (Dec. 2022): 1388–1395, https://doi.org/10.1038/s41563-022-01395-y.

30. P. Fassl, V. Lami, A. Bausch, et al., "Fractional Deviations in Precursor Stoichiometry Dictate the Properties, Performance and Stability of Perovskite Photovoltaic Devices," *Energy & Environmental Science* 11, no. 12 (2018): 3380–3391, https://doi.org/10.1039/C8EE01136B.

31. Z. Hu, Q. An, H. Xiang, et al., "Enhancing the Efficiency and Stability of Triple-Cation Perovskite Solar Cells by Eliminating Excess PbI_2 from the Perovskite/Hole Transport Layer Interface," *ACS Applied Materials & Interfaces* 12, no. 49 (Dec. 2020): 54824–54832, https://doi.org/10.1021/acsami.0c17258.

32. Q. Chen, H. Zhou, T-.B. Song, et al., "Controllable Self-Induced Passivation of Hybrid Lead Iodide Perovskites toward High Performance Solar Cells," *Nano Letters* 14, no. 7 (Jul. 2014): 4158–4163, https://doi.org/10.1021/nl501838y.

33. E. L. Lim and Z. Wei, "A Short Overview of the Lead Iodide Residue Impact and Regulation Strategies in Perovskite Solar Cells," *Journal of Energy Chemistry* 90 (Mar. 2024): 504–510, https://doi.org/10.1016/j.jechem.2023.11.021.

34. A. Farag, P. Fassl, H. Hu, et al., Mitigation of Open-Circuit Voltage Losses in Perovskite Solar Cells Processed over Micrometer-Sized-Textured Si Substrates," *Advanced Function Material* 33, no. 3 (Jan. 2023): https://doi.org/10.1002/adfm.202210758.

35. C. Barugkin, T. Allen, T. K. Chong, T. P. White, K. J. Weber, and K. R. Catchpole-A391, "Light Trapping Efficiency Comparison of Si Solar Cell Textures Using Spectral Photoluminescence," *Optical Express* 23, no. 7 (Apr. 2015): https://doi.org/10.1364/OE.23.00A391.

36. E. M. Tennyson, K. Frohna, W. K. Drake, et al., "Multimodal Microscale Imaging of Textured Perovskite–Silicon Tandem Solar Cells," *ACS Energy Letters* 6, no. 6 (Jun. 2021): 2293–2304, https://doi.org/10.1021/acsenergylett.1c00568.

37. C. Schinke, D. Hinken, J. Schmidt, K. Bothe, and R. Brendel, "Modeling the Spectral Luminescence Emission of Silicon Solar Cells and Wafers," *IEEE Journal of Photovoltaics* 3, no. 3 (Jul. 2013): 1038–1052, https://doi.org/10.1109/JPHOTOV.2013.2263985.

38. Y. Zhao, F. Ma, Z. Qu, et al., "Inactive $(PbI_2)_2$ RbCl Stabilizes Perovskite Films for Efficient Solar Cells," *Science (New York)* 377, no. 6605 (Jul. 2022): 531–534, https://doi.org/10.1126/science.abp8873.

39. T. Unold and L. Gütay, "Photoluminescence Analysis of Thin-Film Solar Cells," in *Advanced Characterization Techniques for Thin Film Solar Cells*, 1st ed., eds. D. Abou-Ras, T. Kirchartz, and U. Rau (Wiley, 2016), pp. 275–297, https://doi.org/10.1002/9783527699025.ch11.

40. M. Stolterfoht, P. Caprioglio, C. M. Wolff, et al., "The Impact of Energy Alignment and Interfacial Recombination on the Internal and External Open-Circuit Voltage of Perovskite Solar Cells," *Energy & Environmental Science* 12, no. 9 (2019): 2778–2788, https://doi.org/10.1039/C9EE02020A.

41. J. Warby, S. Shah, J. Thiesbrummel, et al., "Mismatch of Quasi–Fermi Level Splitting and V_{Oc} in Perovskite Solar Cells," *Advanced Energy Material*, 13, no. 48 (Dec. 2023); https://doi.org/10.1002/aenm.202303135.

42. D. Bi, W. Tress, M. I. Dar, et al., "Efficient Luminescent Solar Cells Based on Tailored Mixed-Cation Perovskites," *Science Advances* 2, no. 1 (Jan. 2016): e1501170, https://doi.org/10.1126/sciadv.1501170.

43. B. Park, N. Kedem, M. Kulbak, et al., "Understanding How Excess Lead Iodide Precursor Improves Halide Perovskite Solar Cell Performance," *Nature Communications* 9, no. 1 (Aug. 2018): 3301, https://doi.org/10.1038/s41467-018-05583-w.

44. G. Tumen-Ulzii, C. Qin, D. Klotz, et al., "Detrimental Effect of Unreacted PbI_2 on the Long-Term Stability of Perovskite Solar Cells," *Advanced Material* 32, no. 16 (Apr. 2020), https://doi.org/10.1002/adma.201905035.

45. J. Liang, X. Hu, C. Wang, et al., "Origins and Influences of Metallic Lead in Perovskite Solar Cells," *Joule* 6, no. 4 (Apr. 2022): 816–833, https://doi.org/10.1016/j.joule.2022.03.005.

46. Y. Gao, H. Raza, Z. Zhang, W. Chen, and Z. Liu, "Rethinking the Role of Excess/Residual Lead Iodide in Perovskite Solar Cells," *Advanced Functional Materials* 33, no. 26 (Jun. 2023): 2215171, https://doi.org/10.1002/adfm.202215171.

47. T. Meier, T. P. Gujar, A. Schönleber, et al., "Impact of Excess PbI_2 on the Structure and the Temperature Dependent Optical Properties of Methylammonium Lead Iodide Perovskites," *Journal of Materials Chemistry C* 6, no. 28 (2018): 7512–7519, https://doi.org/10.1039/C8TC02237B.

48. A. Merdasa, A. Kiligaridis, C. Rehermann, et al., "Impact of Excess Lead Iodide on the Recombination Kinetics in Metal Halide Perovskites," *ACS Energy Letters* 4, no. 6 (Jun. 2019): 1370–1378, https://doi.org/10.1021/acsenergylett.9b00774.

49. M. Saliba, T. Matsui, J. Y. Seo, et al., "Cesium-Containing Triple Cation Perovskite Solar Cells: Improved Stability, Reproducibility and High Efficiency," *Energy & Environmental Science* 9, no. 6 (Jun. 2016): 1989–1997, https://doi.org/10.1039/c5ee03874j.

50. J. C. Sutter, "Advanced Light Management Concepts for Silicon and Perovskite Based Solar Cells: Implementing Tailor-Made Textures in Single-and Multijunction Solar Cell Devices" (*PhD thesis*, Technische Universität Berlin, 2022), https://doi.org/10.14279/depositonce-16580.

Supporting Information

Additional supporting information can be found online in the Supporting Information section. **Supporting Fig. S1:** Thinner perovskite absorber on smooth sinusoidal nanotexture. SEM images of perovskite on (a,b) planar substrate compared with perovskite on (c–f) sinusoidal nanotexture with various dilution ratio creating different perovskite thicknesses along with (g–l) their respective AFM images. **Supporting Fig. S2:** Cross-section energy-dispersive X-ray spectroscopy (EDX) measurement on perovskite absorber layer. Cross-section SEM images of perovskite on (a) planar and (b) 2.0 μm deep inverted pyramids with the EDX-measured areas indicated. (c) Comparison of the resulting EDX spectra of a fully planar perovskite film and the flat top area of the inverted pyramidal texture. (d) EDX spectra of perovskite on flat top areas of the inverted pyramidal textures compared with the bottom valley parts of the pyramids. **Supporting Fig. S3:** Performance characterization of perovskite solar cells on inverted micropyramids. (a) J_{SC}, (b) V_{OC}, (c) fill factor (*FF*), and (d) PCE of the perovskite solar cells on inverted micropyramidal textures compared to planar, fabricated with the same procedure and grouped by pyramid size. (e) Absolute photoluminescence (PL) spectra of best-performing fully textured perovskite solar cells on inverted pyramidal textures from each pyramid sizes and their planar counterpart, along with their peak position written for each spectrum. (f) QFLS calculated from the resulting absolute PL spectra in (e) compared with their respective V_{OC} obtained from *J-V* measurement. **Supporting Fig. S4:** Sample appearances of the perovskite solar cells fabricated on (a) planar substrate, (b) 1.6 μm deep inverted pyramids, (c) 2.0 μm deep inverted pyramids, and (d) 2.3 μm deep inverted pyramids. The two horizontal silver stripes at the top and bottom contact the ITO on the substrate, while the six dumbbell-like silver patches connect the ETL of the individual solar cell pixels. The active area is defined as the overlap of the dumbbell-like patches with the ITO-covered area. Due to some slight variation in active area for different cells from the evaporation process of the silver contact, a shadowing mask is used during *J-V* characterization to ensure accurate measurement result. (e) Illustration of the perovskite solar cell layer stack on glass with textured resist, with light entering from the glass side. **Supporting Fig. S5:** Perovskite with different excess PbI_2 content on planar and inverted pyramids. SEM images of perovskite on (a–c) planar and (d–f) inverted pyramids with pyramids depth of 2.0 μm with different excess PbI_2 content, which are (a,d) 9%, (b,e) 12%, and (c,f) 15%. Absolute PL measurement of perovskite with different excess PbI_2 content grown on (g) planar and (h) 2.0 μm deep inverted pyramids, with the calculated QFLS value of the respective PL spectra indicated for each spectrum. **Supporting Fig. S6:** Performance characterization of perovskite solar cells with different excess PbI_2 content. (a) J_{SC}, (b) fill factor (FF), and (c) PCE of planar and fully textured perovskite solar cells with 9% and 12% of excess PbI_2 content deposited on planar and inverted pyramids. **Supporting Fig. S7:** XRD diffractograms of perovskite single junction solar cells with 12% excess PbI_2. XRD diffractograms of perovskite single junction solar cells with 12% excess PbI_2 content deposited on planar and inverted pyramids with different pyramids sizes with diffraction peak for PbI_2 (001), which appears at 12.7°, appearing only on perovskite on planar substrates.